# Phase-field modeling of fracture in linear thin shells

F. Amiri * D. Millán † Y. Shen‡ T. Rabczuk § M. Arroyo ¶

**Abstract**

We present a phase-field model for fracture in Kirchoff-Love thin shells using the local maximum-entropy (LME) meshfree method. Since the crack is a natural outcome of the analysis it does not require an explicit representation and tracking, which is advantage over techniques as the extended finite element method that requires tracking of the crack paths. The geometric description of the shell is based on statistical learning techniques that allow dealing with general point set surfaces avoiding a global parametrization, which can be applied to tackle surfaces of complex geometry and topology. We show the flexibility and robustness of the present methodology for two examples: plate in tension and a set of open connected pipes.

**Keywords:** phase-field model, meshfree method, thin shells, local maximum entropy, point-set surfaces, manifold learning

## 1 Introduction

The prediction of fracture in thin structures is of major importance in engineering applications such as aircraft fuselages, pressure vessels, automobile components, and castings. Since analytical solutions provide limited information, there has been a keen interest in numerically simulating fracture in thin shells in recent years. However, despite the advances made in modeling fracture for solid bodies [1, 2, 3, 4, 5], fracture in thin bodies remains a challenge due to the complex interplay between cracks and the shell kinematics and geometry.

Non-propagating cracks in plates and shells have been modeled with partition-of-unity methods [6, 7, 8]. These approaches have been restricted to simple geometries. The majority of formulations are based on Mindlin-Reissner theory [9]. There are comparatively fewer methods considering fracture in thin shells [10]. In [11], a shell element based on discrete Kirchhoff theory was proposed assuming through-the-thickness cracks. Later, a shell model with the phantom node method based on edge rotations was proposed [12] for both thin and thick shells, where the crack tip can be located inside an element. A method based

*Insitute for Structure Mechanics, Marienstr. 15, Bauhaus University Weimar, Weimar 99423, Germany. E-mail address: fatemeh.amiri@uni-weimar.de

†School of Civil Engineering of Barcelona (ETSECCPB), Departament de Matemática Aplicada 3 , Universitat Politècnica de Catalunya, Spain. E-mail address: rdanielmillan@gmail.com

‡Laboratori de Càlcul Numèric, Universitat Politècnica de Catalunya (UPC Barcelona-Tech), 08034 Barcelona, Spain. E-mail address: yongxing.shen@upc.edu

§Insitute for Structure Mechanics, Marienstr. 15, Bauhaus University Weimar, Weimar 99423, Germany. Professor School of Civil, Environmental and Architectural Engineering, Korea University. E-mail address: timon.rabczuk@uni-weimar.de

¶School of Civil Engineering of Barcelona (ETSECCPB), Departament de Matemática Aplicada 3 , Universitat Politècnica de Catalunya, Spain. E-mail address: marino.arroyo@upc.edu

on subdivision shell elements and modeling the fracture along the element edges with a cohesive law was proposed in [13]. In [14, 15, 16], a meshfree thin shell model for static and dynamic fracture was presented.

Most of above methods are based on discrete crack models that require explicitly (or sometimes implicitly [17]) tracking the crack path. Furthermore, many of the approaches are applied to simple geometries such as plates, or spherical and cylindrical geometries [18, 19, 12, 20]. Towards a general, flexible and robust methodology to deal with fracture in Kirchhoff-Love shells, we propose here treating fracture with a phase-field model and discretizing the coupled thin-shell/phase-field equations with a recently proposed meshfree method for partial differential equations on manifolds of complex geometry and topology [21, 22].

Phase-field methods are widely used in science and engineering to model a variety of physics [23, 24, 25, 26]. The extension of this method for fracture in solids was introduced in [27, 28], where the brittle crack propagation problem was regularized and recast as a minimization problem. In the phase-field approach, discontinuities are not introduced into the displacement field or geometrically described. Instead, a continuous field governed by a partial differential equation models cracks and their evolution. Crack propagation does not require evaluating stress intensity factors. This method naturally deals with crack nucleation, branching and coalesce result in a simple implementation. Its main drawback is its high computational cost. The crack zone is controlled by a regularization parameter. As this regularization parameter converges to zero, the phase field model converges to a discrete crack model.

Dealing computationally with the Kirchhoff-Love theory is challenging because second derivatives of the displacement field appear in the weak form, and therefore a Galerkin method requires $C^1-$continuous basis functions. This can be overcome by discretizing the director field or introducing rotational degrees of freedom [29, 30, 31], or by considering more elaborate variational formulations such as in discontinuous Galerkin methods [32, 33]. Instead, here we focus on methods relying on smooth basis functions. Finite element methods with high order continuity have been proposed, either based on subdivision surfaces [13, 34] or on isogeometric analysis [35, 36, 37]. The higher order continuity of the meshfree basis functions has also been exploited for this purpose [14, 15], but since meshfree basis functions are defined in physical space, these methods were applied to simple geometries with a single parametric patch. Recently, nonlinear manifold learning techniques have been exploited to parametrize 2D sub-domains of a point-set surface, which are then used as parametric patches and glued together with a partition of unity [38, 21]. Here, we combine this methodology with local maximum-entropy (LME) meshfree approximants [39, 40, 5] because of their smoothness, robustness, and relative ease of quadrature compared with other meshfree approximants.

The paper is organized as follows. Section 2 describes the representation of general surfaces represented by a set of scattered points [21]. In Section 3, we review the Kirchhoff–Love theory of thin shells. In Section 4, we introduce a phase-field model for fracture in thin shells. The Galerkin discretization is also presented in this section. In Section 5 we demonstrate the capabilities of the method through two numerical examples. Some concluding remarks are given in Section 6.

## 2 Numerical representation of the surfaces

To illustrate the method considered here for numerically representing surfaces defined by a set of scattered points, we refer to Fig. 1. As noted in [41], a fundamental difficulty in defining basis functions and performing calculations on a surface, as compared to open sub-sets in Euclidean space, is the absence in general of a single parametric domain. A simple example is the sphere, which does not admit a single singularity-free parametrization. Mesh-based methods, consisting of a collection of local parametrizations from the parent element to the physical elements, do not have any difficulty in this respect at the expense of reduced smoothness across the element boundaries or the need for special techniques to recover inter-element smoothness.

In meshfree methods, such a natural parametric domain is not available, and the description of surfaces with a topology different to that of an open set in $\mathbb{R}^2$, such as a sphere (A) or a set of connected pipes ( B), is a challenge. Even for surfaces homeomorphic to open two-dimensional sets, such as that depicted in (C), the geometric complexity can make it very difficult to produce well-behaved global parametrizations. For these reasons, the method we follow here proceeds in four steps: (1) We first partition the set of scattered points into subsets. (2) For each subset, the geometric structure of the surface is detected by dimensionality reduction methods and its points are embedded in 2D. (3) The 2D embedding then serves as a local parametric patch, and a local parametrization of the surface using smooth meshfree LME approximants is defined. (4) Finally, the different patches are glued together by means of a partition of unity.

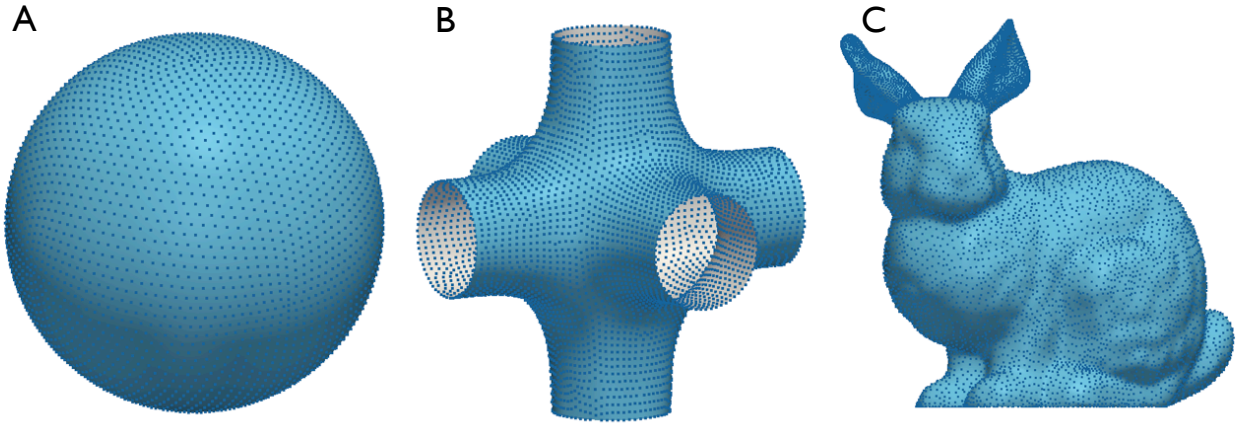


Figure 1: Three point-set surfaces that require partitioning for different reasons: (A) and (B) for their non-trivial topology, and (C) for its complex geometry.

Consider a smooth surface $\mathcal{M}$ embedded in $\mathbb{R}^3$ and represented by a set of (control) points $P = \{\boldsymbol{P}_1, \boldsymbol{P}_2, \ldots, \boldsymbol{P}_N\} \subset \mathbb{R}^3$. The goal is to numerically represent $\mathcal{M}$ from $P$ and make computations on it. We consider another set $Q = \{\boldsymbol{Q}_1, \boldsymbol{Q}_2, \ldots, \boldsymbol{Q}_M\} \subset \mathbb{R}^3$ with fewer point, typically a subset of $P$ but not necessarily. We call the points of this set geometric markers. For simplicity, we will denote the points in $P$ and its associated objects with a lower case subindex, e.g. $\boldsymbol{P}_a$, for $a = 1, 2, \ldots, N$, and the geometric markers in $Q$ and its associated objects with an upper case subindex, e.g. $\boldsymbol{Q}_A$, for $A = 1, 2, \ldots, M$.

We partition these geometric markers into $L$ groups. These $L$ groups of geometric markers can be represented with index sets $\mathcal{I}_\kappa, \kappa = 1, \ldots, L$ with $\cup_{\kappa=1}^{L} \mathcal{I}_\kappa = \{1, 2, \ldots, M\}$ and $\mathcal{I}_\kappa \cap \mathcal{I}_\iota = \emptyset$ such that $\kappa \neq \iota$. As it will become clear below, there is a one-to-one correspondence between these groups of geometric markers and the local parameterizations of the surface, which here we refer as patches.

We consider a Shepard partition of unity associated with the geometric markers. Given a set of non-negative reals $\{\beta_A\}_{A=1,2,\ldots,M}$, we define the Shepard partition of unity with Gaussian weight associated to the set $Q$ as

$$w_A(\boldsymbol{x}) = \frac{\exp(-\beta_A \left|\boldsymbol{x} - \boldsymbol{Q}_A\right|^2)}{\sum_{B=1}^{M} \exp(-\beta_B \left|\boldsymbol{x} - \boldsymbol{Q}_B\right|^2)}. \tag{1}$$

To obtain a coarser partition of unity representative of a partition, we aggregate the partition of unity functions as

$$\psi_\kappa(\boldsymbol{x}) = \sum_{A \in \mathcal{I}_\kappa} w_A(\boldsymbol{x}). \tag{2}$$

These functions form a partition of unity in $\mathbb{R}^D$, and consequently also in $\mathcal{M}$. We consider the index sets of all control points influencing each patch, $\mathcal{J}_\kappa$, with $\cup_{\kappa=1}^{L} \mathcal{J}_\kappa = \{1, 2, \ldots, N\}$, but now $\mathcal{J}_\kappa \cap \mathcal{J}_\iota \neq \emptyset$ due to the overlap between patch partition of unity functions. Roughly speaking, these sets are $\{a \mid \boldsymbol{P}_a \in \sup \psi_\kappa\}$, slightly enlarged so that the patch parameterization is smooth on the boundary of the support of $\psi_\kappa$.

For each patch, through a nonlinear dimensionality reduction technique applied to the set of control points $P_\kappa = \{\boldsymbol{P}_a\}_{a\in\mathcal{J}_\kappa} \subset \mathbb{R}^3$, we obtain a two-dimensional embedding of these points, represented by the set $\Xi_\kappa = \{\boldsymbol{\xi}_a\}_{a\in\mathcal{J}_\kappa} \subset \mathbb{R}^2$. The two-dimensional region defined by these points is a convenient parametric space for the corresponding patch. It is important to note that the embedded points are in general unstructured, and that, although here $d = 2$, the methodology is applicable to higher dimensional embedded manifolds unlike mesh based techniques.

The patch parametrizations often need to be smooth, here because of the requirements of the Kirchhoff-Love theory. We consider here LME basis functions. See [39, 40, 38] for the LME formulation, properties, and the evaluation of the basis functions and their derivatives. Then, let $p_a(\boldsymbol{\xi})$ denote the LME approximants associated to the point-set $\Xi_\kappa$ on a domain $\mathscr{A}_\kappa \subset \mathbb{R}^2$, a subset of the convex hull of the reduced node set conv $\Xi_\kappa$. We locally parameterize the manifold in this patch as

$$\begin{aligned} \boldsymbol{\varphi}_\kappa : \mathscr{A}_\kappa &\longrightarrow \mathbb{R}^3 \\ \boldsymbol{\xi} &\longmapsto \sum_{a\in\mathcal{J}_\kappa} p_a(\boldsymbol{\xi})\, \boldsymbol{P}_a. \end{aligned} \tag{3}$$

Consider a function $f$ over a surface $\mathcal{M}$, $f : \mathcal{M} \to \mathbb{R}$. The integral of this function over the surface can be split into integrals over the patches invoking the partition of unity

$$\int_{\mathcal{M}} f(\boldsymbol{x})\, d\mathcal{M} \simeq \sum_{\kappa=1}^{L} \int_{\mathscr{A}_\kappa} \psi_\kappa(\boldsymbol{\varphi}_\kappa(\boldsymbol{\xi}))\, f(\boldsymbol{\varphi}_\kappa(\boldsymbol{\xi}))\, J_\kappa(\boldsymbol{\xi})\, d\boldsymbol{\xi}, \tag{4}$$

where $J_\kappa = \sqrt{\det\left[(D\boldsymbol{\varphi}_\kappa)^T D\boldsymbol{\varphi}_\kappa\right]}$ is the Jacobian determinant of the parameterization. In this way, similarly to finite element methods, we have split the integral into local contributions, which can be evaluated using local parameterizations. Each patch integral can be approximated by numerical quadrature on the local parametric space, for instance we resort to Gauss quadrature on a support triangulation defined over $\Xi_\kappa$.

# 3 Thin shell model

In this section, we review the mechanics of thin shells [42, 43], based on a geometrically exact formulation presented in [30, 44]. We restrict our attention to the Kirchhoff–Love kinematical assumption of shells, which states that the material line orthogonal to the middle surface in the undeformed configuration remains straight, unstretched and always orthogonal to the middle surface during the deformations. Furthermore, we follow the usual convention for Latin and Greek indices, referring to Cartesian and curvilinear coordinates, respectively (i.e. $i = 1, 2, 3$; $\alpha = 1, 2$). A comma denotes partial derivatives, subscripts refer to covariant components, and superscripts denote contravariant components.

## 3.1 Kinematics of the shell

We consider a shell with a middle surface $\Omega$, defined by $\boldsymbol{\varphi}$ which is a mapping from the parametric space of $\mathbb{R}^2$, denoted by $\mathscr{A}$, into $\Omega$. Assume $\boldsymbol{t}$ is a field of unit vectors (a field of directors). Thus, the thin shell

body $\mathscr{S} \subset$ in three dimension can be described by the pair $(\boldsymbol{\varphi}, \boldsymbol{t})$, see Fig. 2. Additionally, the subscript 0 denotes quantities in the reference configuration, for instance $\boldsymbol{\varphi}_0$ parametrizes the reference middle surface. We assume the thickness $t$ of the shell to be uniform for simplicity, and also we assume that the change in shell thickness after deformation is negligible. Then, the thin shell body $\mathscr{S}$ is given by

$$\mathscr{S} = \left\{ \boldsymbol{\Phi} \in \mathbb{R}^3 |\ \boldsymbol{\Phi} = \boldsymbol{\varphi}(\xi^1, \xi^2) + \xi\ \boldsymbol{t}(\xi^1, \xi^2),\ \ -\frac{t}{2} \leq \xi \leq \frac{t}{2},\ (\xi^1, \xi^2) \in \mathscr{A} \right\}, \tag{5}$$

where $\mathscr{A} \subset \mathbb{R}^2$ is the parametric space for the middle surface. Hence, the configuration $\boldsymbol{\Phi}$ is a mapping from a parametric domain $\mathscr{A} \times [-t/2, t/2]$ into $\mathbb{R}^3$. The coordinates $\{\xi^1, \xi^2, \xi^3\}$ (where $\xi = \xi^3$) describe this parametric domain, which corresponding global Cartesian basis of these coordinates is $\{\boldsymbol{E}_k\}$. The area element of the middle surface can be computed as $d\Omega = \bar{j}\ d\xi^1 d\xi^2$, where $\bar{j} = \left|\boldsymbol{\varphi}_{,1} \times \boldsymbol{\varphi}_{,2}\right|$.

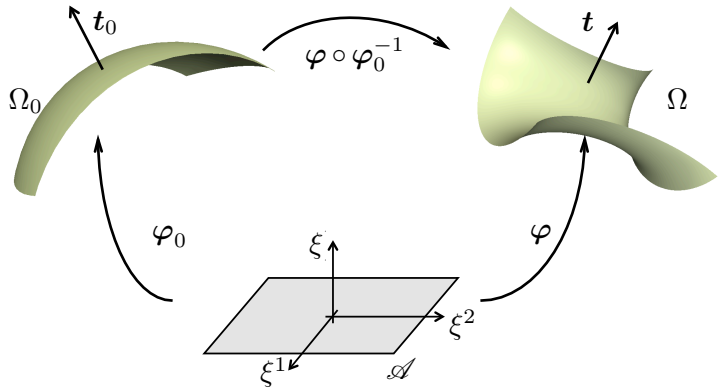


Figure 2: Reference and the deformed configurations of the middle shell surface.

The convective basis vectors $\boldsymbol{g}_i$ can be defined by the tangent map as

$$\nabla\Phi = \frac{\partial \boldsymbol{\Phi}}{\partial \xi^i} \otimes \boldsymbol{E}^i = \boldsymbol{g}_i \otimes \boldsymbol{E}^i,$$

with $\boldsymbol{g}_\alpha = \frac{\partial \boldsymbol{\Phi}}{\partial \xi^\alpha} = \boldsymbol{\varphi}_{,\alpha} + \xi\ \boldsymbol{t}_{,\alpha}$ and $\boldsymbol{g}_3 = \frac{\partial \boldsymbol{\Phi}}{\partial \xi} = \boldsymbol{t}$. The covariant components of the metric tensor in convected coordinates are given by $g_{ij} = \boldsymbol{g}_i \cdot \boldsymbol{g}_j$. The difference between the metric tensors of the undeformed and deformed configurations of the shell is measured by the Green–Lagrange strain tensor, i.e.

$$E_{ij} = \frac{1}{2}\left(g_{ij} - g_{0ij}\right) = \frac{1}{2}(\boldsymbol{\Phi}_{,i} \cdot \boldsymbol{\Phi}_{,j} - \boldsymbol{\Phi}_{0,i} \cdot \boldsymbol{\Phi}_{0,j}).$$

According to the Kirchhoff–Love theory of thin shells, we constrain the deformed director $\boldsymbol{t}$ to coincide with the unit normal of the deformed middle surface of the shell, i.e.

$$\boldsymbol{t} = \frac{\boldsymbol{\varphi}_{,1} \times \boldsymbol{\varphi}_{,2}}{\bar{j}}, \quad \boldsymbol{\varphi}_{,\alpha} \cdot \boldsymbol{t} = 0, \quad |\boldsymbol{t}| = 1, \quad \boldsymbol{t} \cdot \boldsymbol{t}_{,\alpha} = 0.$$

We assume that the deformation field for the shell is restricted to account only for small displacement. For more details, refer to [38, 21] . With the Kirchhoff–Love and the small deformation hypothesis, the only remaining non-zero components of the Green–Lagrange strain tensor are

$$E_{\alpha\beta} \quad = \varepsilon_{\alpha\beta} + \xi\ \rho_{\alpha\beta}, \tag{6}$$

where $\varepsilon_{\alpha\beta} = \frac{1}{2}(\boldsymbol{\varphi}_{,\alpha}\cdot\boldsymbol{\varphi}_{,\beta} - \boldsymbol{\varphi}_{0,\alpha}\cdot\boldsymbol{\varphi}_{,\beta})$ is the membrane strain tensor and $\rho_{\alpha\beta} = \boldsymbol{\varphi}_{,\alpha}\cdot\boldsymbol{t}_{,\beta} - \boldsymbol{\varphi}_{0,\alpha}\cdot\boldsymbol{t}_{0,\beta}$ is a tensor that measures the bending or change in curvature of the shell. Thus, Kirchhoff–Love kinematic assumption leads to a formulation of the shell exclusively in terms of the middle surface.

### 3.2 Thin shell potential energy

The potential energy of an elastic thin shell body under Kirchhoff–Love assumptions can be expressed by the functional

$$\Pi[\boldsymbol{u}] = \int_{\Omega_0} \mathcal{W}(\boldsymbol{u})\; d\Omega_0 + \Pi_{\texttt{ext}}[\boldsymbol{u}], \tag{7}$$

where $\Omega_0$ is the reference middle surface of the thin shell body, $\mathcal{W}$ is an internal energy density per unit area, and $\Pi_{\texttt{ext}}$ is the potential energy of the external loads.

For an isotropic Kirchhoff–St. Venant elastic material the internal energy density follows as

$$\mathcal{W} = \frac{1}{2}C^{\alpha\beta\gamma\delta}\left(t\,\varepsilon_{\alpha\beta}\varepsilon_{\gamma\delta} + \frac{t^3}{12}\rho_{\alpha\beta}\rho_{\gamma\delta}\right),$$

with

$$C^{\alpha\beta\gamma\delta} = \frac{E}{(1-\nu^2)}\left[\nu a_0^{\alpha\beta}a_0^{\gamma\delta} + \frac{1}{2}(1-\nu)\left(a_0^{\alpha\gamma}a_0^{\beta\delta} + a_0^{\alpha\delta}a_0^{\beta\gamma}\right)\right],$$

where we have introduced the first fundamental form $a_{\alpha\beta} = \boldsymbol{\varphi}_{,\alpha}\cdot\boldsymbol{\varphi}_{,\beta}$ expressed in convected components, with $a_0^{\alpha\gamma}(a_0)_{\gamma\beta} = \delta^{\alpha}_{\beta}$. $E$ is the Young's modulus, and $\nu$ is the Poisson's ratio [38, 21].

The external potential energy expressed in the reference middle surface states as

$$\Pi_{\texttt{ext}}[\boldsymbol{u}] = -\int_{\Omega_0}\boldsymbol{q}\cdot\boldsymbol{u}\; d\Omega_0 - \int_{\partial\Omega_0}\boldsymbol{h}\cdot\boldsymbol{u}\; d\eta_0,$$

where $\boldsymbol{q}$ is the external body load per unit area, $\boldsymbol{h}$ the forces per unit length applied on the boundary of the middle surface, and $d\eta_0$ is the line element of the boundary of the middle surface.

## 4 Phase-field model for thin shell

Let us consider a thin shell model that assumes the phase-field to be constant across the thickness. The total potential energy functional for a thin shell body with crack (elastic and surface energies) is given by

$$\Pi[\boldsymbol{u}, \upsilon] = \int_{\Omega_0}(\upsilon^2+\epsilon)\mathcal{W}(\boldsymbol{u})\; d\Omega_0 + \int_{\Omega_0} G_c\; t\left[\frac{(1-\upsilon)^2}{4\ell} + \ell|\nabla\upsilon|^2\right] d\Omega_0 + \Pi_{\texttt{ext}}[\boldsymbol{u}], \tag{8}$$

where $\upsilon$ is phase-field describing uniform cracks through the thickness, $G_c$ is the critical energy release rate, or surface energy, in Griffith's theory, and $\ell$ is a positive regularization constant to regulate the size of the fracture zone. It was shown by [28] for bulk materials, that when $\ell$ tends to zero, the phase-field approximation of the fracture energy converges to the fracture energy.

For an accurate discretized surface energy, the nodal spacing of the discretization $h$ should be smaller than the regularization parameter $\ell$ , i.e. $h/\ell \ll 1$. Moreover, the crack area, which is controlled by $\ell$, should be smaller than the domain area, in order to approximate the sharp-interface model. Numerical experiments illustrate that setting $2h \sim \ell$ still gives reasonable results. However, the computed surface energy will be slightly overestimated [28, 45].

In this model, the energy is released due to fracture in both tension and compression. This limits the application of the presented model to problems with pure tensile loading. In the future, we will separate the positive and the negative part of the stored energy based on the spectral decomposition of the strain tensor [46].

The natural boundary conditions are used for $\upsilon$. The crack is assumed to be traction-free. In order to satisfy this condition the internal energy density $\mathcal{W}$ is multiplied by the jump set function $(\upsilon^2+\epsilon)$. The parameter $\epsilon \ll 1$ is introduced to avoid the singularity of disappearing internal energy density when the phase-field parameter is zero. In this model, cracks can propagate, branch and merge but can not reverse, whereas the last feature is reached by imposing $\upsilon^i \leqslant \upsilon^{i-1}$, such that $\upsilon^{i-1}$ and $\upsilon^i$ are the phase-field parameters at step $i-1$ and $i$ [47].

The first variation of the functional $\Pi[\boldsymbol{u},\upsilon]$ is given by

$$\delta\Pi = \delta\Pi_{\texttt{int}} + \delta\Pi_{\texttt{ext}} = 0.$$

Since the variations $\delta\boldsymbol{u}$ and $\delta\upsilon$ are independent, the above expression leads to two decoupled equations

$$\delta\Pi[\boldsymbol{u},\upsilon,\delta\boldsymbol{u}] = \int_{\mathscr{A}} (\upsilon^2+\epsilon) C^{\alpha\beta\gamma\delta}\left(t\,\varepsilon_{\gamma\delta}(\boldsymbol{u})\,\varepsilon_{\alpha\beta}(\delta\boldsymbol{u}) + \frac{t^3}{12}\,\rho_{\gamma\delta}(\boldsymbol{u})\,\rho_{\alpha\beta}(\delta\boldsymbol{u})\right)\bar{j}_0\; d\xi^1 d\xi^2 + \delta\Pi_{\texttt{ext}}[\delta\boldsymbol{u}] = 0, \tag{9}$$

$$\delta\Pi[\boldsymbol{u},\upsilon,\delta\upsilon] = \int_{\mathscr{A}} 2\upsilon\delta\upsilon\mathcal{W}(\boldsymbol{u})\;\bar{j}_0\; d\xi^1 d\xi^2 + 2\int_{\mathscr{A}} t\,G_c\left(-\frac{(1-\upsilon)\delta\upsilon}{4\ell} + \ell\nabla\upsilon\nabla(\delta\upsilon)\right)\bar{j}_0\; d\xi^1 d\xi^2 = 0, \tag{10}$$

with the external virtual work

$$\delta\Pi_{\texttt{ext}}[\delta\boldsymbol{u}] = -\int_{\mathscr{A}} \boldsymbol{q}\cdot\delta\boldsymbol{u}\;\bar{j}_0\; d\xi^1 d\xi^2 - \int_{\partial\mathscr{A}} \boldsymbol{h}\cdot\delta\boldsymbol{u}\,\|\boldsymbol{\varphi}_{0,t}\|\,d\eta_\xi. \tag{11}$$

With the strategy presented in Section 2, we can split the expressions stated by the principle of virtual work into partition contributions, that is

$$\begin{aligned}\delta\Pi[\boldsymbol{u},\upsilon,\delta\boldsymbol{u}] = &\sum_{\kappa=1}^{L}\int_{\mathscr{A}_\kappa}\left[(\upsilon^2+\epsilon)C^{\alpha\beta\gamma\delta}\left(t\,\varepsilon_{\gamma\delta}(\boldsymbol{u})\,\varepsilon_{\alpha\beta}(\delta\boldsymbol{u}) + \frac{t^3}{12}\,\rho_{\gamma\delta}(\boldsymbol{u})\,\rho_{\alpha\beta}(\delta\boldsymbol{u})\right)\bar{j}_0\right]_\kappa (\psi_\kappa\circ\boldsymbol{\varphi}_0)\; d\xi^1 d\xi^2 \\ &- \sum_{\kappa=1}^{L}\int_{\mathscr{A}_\kappa}\left[\boldsymbol{q}\cdot\delta\boldsymbol{u}\;\bar{j}_0\right]_\kappa (\psi_\kappa\circ\boldsymbol{\varphi}_0)\; d\xi^1 d\xi^2 - \sum_{\kappa=1}^{L}\int_{\partial\mathscr{A}_\kappa}\left[\boldsymbol{h}\cdot\delta\boldsymbol{u}\,\|\boldsymbol{\varphi}_{0,t}\|\right]_\kappa (\psi_\kappa\circ\boldsymbol{\varphi}_0)\; d\eta_\xi = 0,\end{aligned} \tag{12}$$

and

$$\begin{aligned}\delta\Pi[\boldsymbol{u},\upsilon,\delta\upsilon] = &\sum_{\kappa=1}^{L}\int_{\mathscr{A}_\kappa}\left[\left(2\mathcal{W}(\boldsymbol{u}) + \frac{t\,G_c}{2\ell}\right)\upsilon\,\delta\upsilon\,\bar{j}_0\right]_\kappa (\psi_\kappa\circ\boldsymbol{\varphi}_0)\; d\xi^1 d\xi^2 \\ &+ \sum_{\kappa=1}^{L}\int_{\mathscr{A}_\kappa} 2\left[t\,G_c\,\ell\left(\frac{\partial\upsilon}{\partial\xi^\alpha} g^{\alpha\beta}\frac{\partial(\delta\upsilon)}{\partial\xi^\beta}\right)\bar{j}_0\right]_\kappa (\psi_\kappa\circ\boldsymbol{\varphi}_0)\; d\xi^1 d\xi^2 \\ &- \sum_{\kappa=1}^{L}\int_{\mathscr{A}_\kappa}\left[\frac{t\,G_c}{2\ell}\delta\upsilon\,\bar{j}_0\right]_\kappa (\psi_\kappa\circ\boldsymbol{\varphi}_0)\; d\xi^1 d\xi^2 = 0,\end{aligned} \tag{13}$$

such that $g^{\alpha\gamma}g_{\gamma\beta} = \delta^\alpha_\beta$. Here, $[\cdot]_\kappa$ means that the expression within the brackets is evaluated with the $\kappa$-th partition approximation of the undeformed middle surface.

### 4.1 Galerkin discretization

We consider now the discrete equilibrium equations for a shell whose middle surface in the reference configuration is numerically represented with the procedure described before, in terms of a set of nodes $P_0 = \{\boldsymbol{P}_{01}, \ldots, \boldsymbol{P}_{0N}\}$, and a set of $L$ patches. We follow a total Lagrangian approach, with the same parameter space and basis functions for the reference and deformed configurations. Let $\boldsymbol{\varphi}_{0\kappa}$ be the reference configuration mapping for the middle surface of a specific part $\kappa$, defined over the parametric space $\mathscr{A}_\kappa$

$$\boldsymbol{\varphi}_{0\kappa}(\boldsymbol{\xi}) = \sum_{a \in \mathcal{J}_\kappa} p_a(\boldsymbol{\xi})\ \boldsymbol{P}_{0a}, \tag{14}$$

We represent the deformed configuration in a given partition $\kappa$ as

$$\boldsymbol{u}_\kappa(\boldsymbol{\xi}) = \sum_{a \in \mathcal{J}_\kappa} p_a(\boldsymbol{\xi})\ \boldsymbol{u}_a, \tag{15}$$

and the approximation of the phase-field parameter, $\upsilon$, as

$$\upsilon_\kappa(\boldsymbol{\xi}) = \sum_{a \in \mathcal{J}_\kappa} q_a(\boldsymbol{\xi})\ \upsilon_a. \tag{16}$$

Where $p_a(\boldsymbol{\xi})$ and $q_a(\boldsymbol{\xi})$ are LME basis functions. Virtual displacements and virtual phase-field parameters are represented likewise. A simple calculation yields the Galerkin stiffness matrix. The interaction between nodes $a$ and $b$ is given by

$$\boldsymbol{K}^{ab}_{\boldsymbol{u}} = \sum_{\kappa=1}^{L} \int_{\mathscr{A}_\kappa} \left[ (\upsilon^2 + \epsilon) \left( t\, \boldsymbol{M}^{a\,T} \boldsymbol{C} \boldsymbol{M}^b + \frac{t^3}{12} \boldsymbol{B}^{a\,T} \boldsymbol{C} \boldsymbol{B}^b \right) \bar{j}_0 \right]_\kappa (\psi_\kappa \circ \boldsymbol{\varphi}_0)\ d\xi^1 d\xi^2,$$

Where $\boldsymbol{M}^a$ and $\boldsymbol{B}^a$ are the membrane and bending strain-displacement matrices for the $a$-th node. Note that $\boldsymbol{M}^a, \boldsymbol{B}^a \in \mathbb{R}^{3\times 3}$, see [38] for a detailed description. The force contribution of the $a$-th node is

$$\boldsymbol{f}^a_{\boldsymbol{u}} = \sum_{\kappa=1}^{L} \int_{\mathscr{A}_\kappa} \left[ \boldsymbol{q}\, p_a\, \bar{j}_0 \right]_\kappa (\psi_\kappa \circ \boldsymbol{\varphi}_0)\ d\xi^1 d\xi^2 + \sum_{\kappa=1}^{L} \int_{\partial\mathscr{A}_\kappa} \left[ \boldsymbol{h}\, p_a\, \left\| \boldsymbol{\varphi}_{0,t} \right\| \right]_\kappa (\psi_\kappa \circ \boldsymbol{\varphi}_0)\ d\eta_\xi.$$

Finally, the phase-field stiffness matrix is

$$\boldsymbol{K}^{ab}_{\upsilon} = \sum_{\kappa=1}^{L} \int_{\mathscr{A}_\kappa} \left[ \left( 2\mathcal{W}(\boldsymbol{u}) + \frac{t\, G_c}{2\ell} \right) q_a\, q_b\, \bar{j}_0 + 2\,\ell\, t\, G_c\, q_{a,\alpha}\, q_{b,\beta}\, g^{\alpha\beta}\, \bar{j}_0 \right]_\kappa (\psi_\kappa \circ \boldsymbol{\varphi}_0)\ d\xi^1 d\xi^2, \tag{17}$$

and the right hand side for phase-field is

$$\boldsymbol{f}^a_{\upsilon} = \sum_{\kappa=1}^{L} \int_{\mathscr{A}_\kappa} \frac{t\, G_c}{2\ell} \left[ q_a\, \bar{j}_0 \right]_\kappa (\psi_\kappa \circ \boldsymbol{\varphi}_0)\ d\xi^1 d\xi^2. \tag{18}$$

The Dirichlet displacement and rotation boundary conditions are imposed with Lagrange multipliers, the interested reader is referred to [48, 49, 38, 50].

# 5 Numerical examples

As it was discussed in [39], the locality of the LME basis functions smoothness depends on a nondimensional parameter $\gamma$. The large value of $\gamma$ leads to sharper shape functions, while the small value results wider shape functions. Phase field model was introduced based on standard FEM shape functions, so using smooth shape function will not capture the discontinuity. Whereas the main idea of modeling the thin shell from scattered points, as explained above, is to use smooth shape functions by choosing $\gamma$ as a small value for thin shell, we have smoother shape functions. Here, we first test the efficiency of the introduced method through a simple $2D$ example to show a suitable $\gamma$ for the LME shape functions used in this model. In the second example we consider a thin shell structure with a complex topology, in order to indicate the ability of the introduced method in modeling fracture in complex structures.

## 5.1 Single edge notch tensile

To get a better understanding of the proposed methodology, we consider a well studied benchmark example of $2D$ solid under plane stress state [51, 52]. The plane is a square of edge length $L = 1$ mm, under pure tension with initial crack (see sketch in Fig. 3). The crack is replaced at the middle of the plane edge with length $L/2$ and width of $2h$. The elastic constants are chosen as $E = 10^9$ N/mm$^2$ and $\nu = 0.3$, the critical energy release rate as $G_c = 1$ N/mm and $\epsilon = 10^{-6}$. The constant displacement increments $\Delta u = 0.5 \times 10^{-6}$ mm, are used for each step of computation.

The results are indicated in Figs. 4, 5, 6 and 7 for a uniform discretization with nodal spacing $h = 0.005$. The crack path is illustrated in Fig. 4. As it was expected , the crack propagates in a symmetry path [46]. For fixed regularization parameter $\ell = 0.05$ mm, the influence of the different values of $\gamma$ for the LME approximants, is analyzed. Fig. 5 depicts the load-deflection curves for FEM and LME with different values of $\gamma$. The same results are observed for LME with $\gamma \geq 1.8$ and FEM, while $\gamma \leq 0.8$ gives less accurate result, due to the wider and smoother LME shape functions. Therefore, the LME results converge to the standard FEM results as $\gamma$ increases [39]. The subsequent study analyzes the influence of the critical energy release rate $G_c$. The energy release rate, $G$, is the rate of change in potential energy with crack area. The crack extension occurs when $G$ reaches a critical value $G_c$. Hence, as $G_c$ decreases the material are more brittle and reaction force is lower. Figs. 6, 7 illustrate the load-deflection curves for different values of $Gc$, $\gamma = 1.8$, $\ell = 0.05$ and $\ell = 0.025$. It is obvious from these figures as $G_c$ increases the area under the load-deflection curve appends. Fig. 8 indicates load-deflection curves for different discretization with nodal spacing $h = 0.0204, 0.0101, 0.005$. In this figure for fine mesh, $h \leq 0.0101$, the results are mesh-independent, which conform the results obtained by [46].

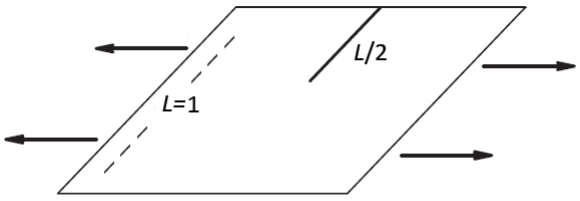


Figure 3: Square plate of side length $L = 1$ mm with initial crack of length $L/2$ under pure tension.

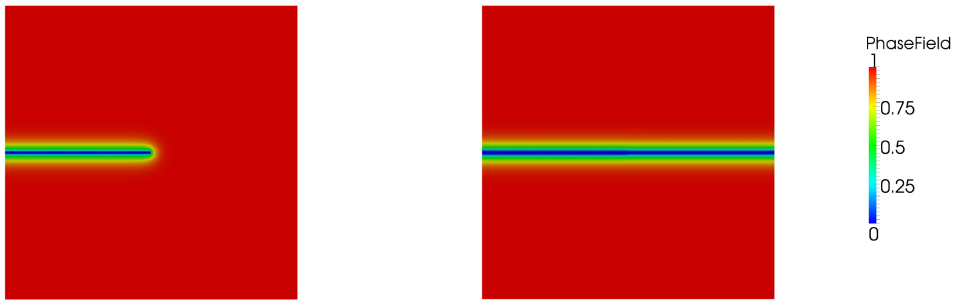


Figure 4: (Left) initial phase-field parameter values with initial crack width of $2h$, (right) phase-field solution of the plate for the final state after full breaking.

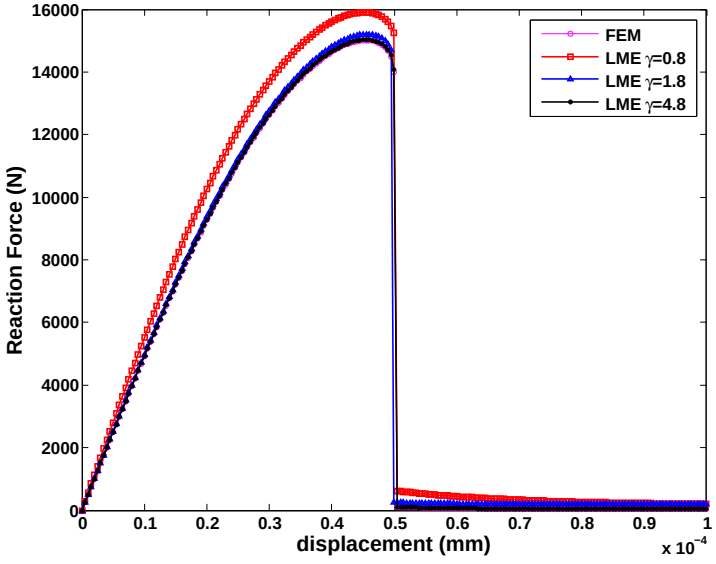


Figure 5: Load-deflection curves for FEM and LME with $\gamma = 0.8, 1.8$ and $4.8$.

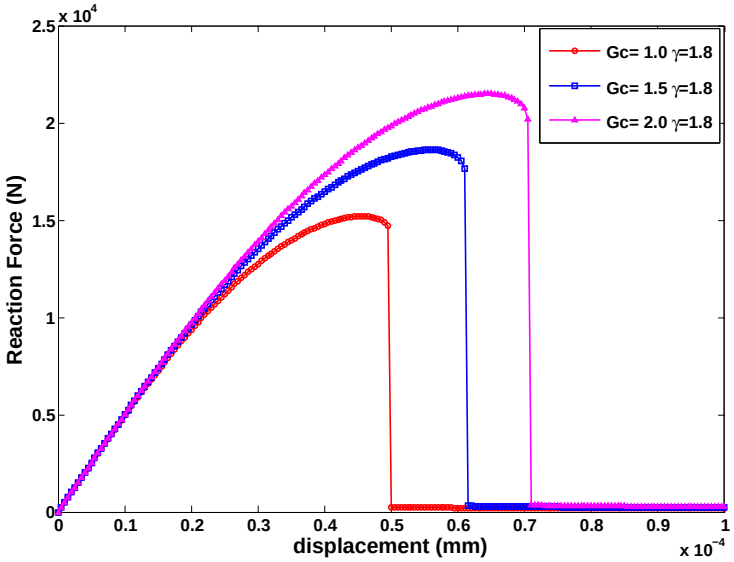


Figure 6: Load-deflection curves for $h = 0.005$, $G_c = 1.0, 1.5, 2.0$ N/mm, $\ell = 0.05$ mm and $\gamma = 1.8$.

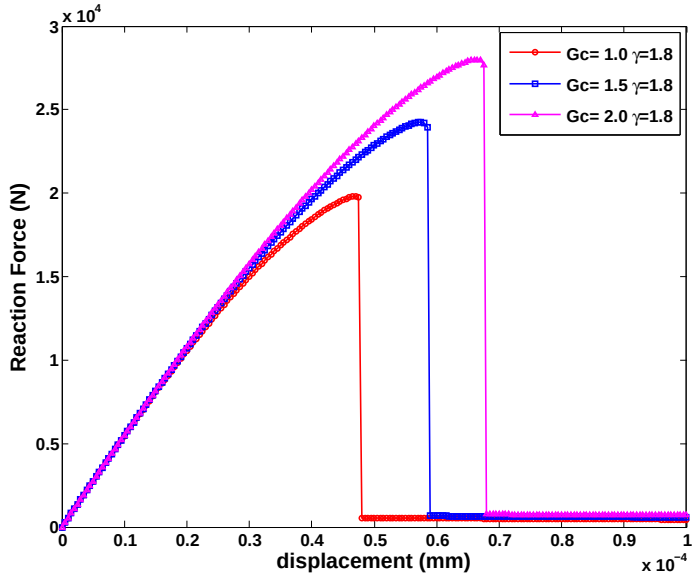


Figure 7: Load-deflection curves for $h = 0.005$, $G_c = 1.0, 1.5, 2.0$ N/mm, $\ell = 0.025$ mm and $\gamma = 1.8$.

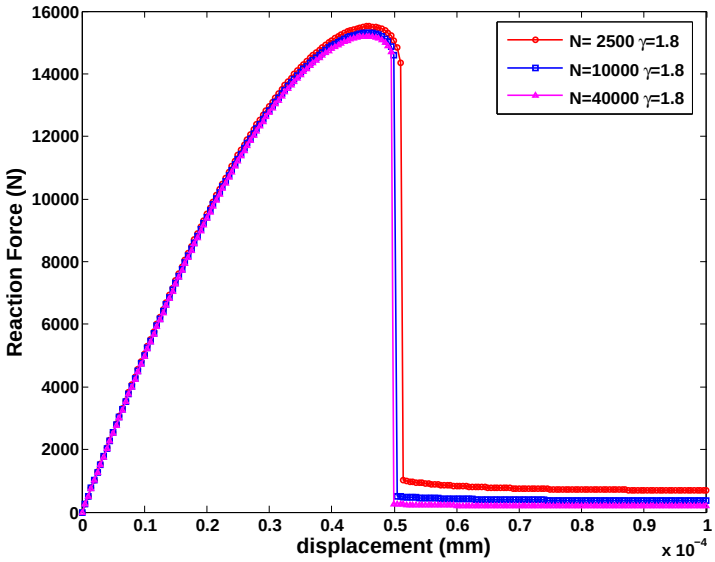


Figure 8: Load-deflection curves for $h = 0.0204, 0.0101, 0.005$, $G_c = 1.0$ N/mm, $\ell = 0.05$ mm and $\gamma = 1.8$.

## 5.2 Connected pipes pulling

In this example we show the flexibility and robustness of the present methodology to deal with a thin shell of complex topology and complex crack path. Figure 9 shows the surface, consisting of a set of six connected open pipes. The boundary curve at the bottom is clamped, whereas the top boundary curve is incrementally displaced in the upward $(0, 0, 1)$ direction. Material parameters have been selected as $E = 10^7$ N/mm$^2$ and $\nu = 0.3$, $G_c = 1$ N/mm, while the thickness is $t = 0.005$ mm. The discretization of the geometry (geometric markers) and the control points consists of two arrangements of 25668 and 100380 unstructured set of points respectively. The original coarse point-set has been obtained from the MATLAB central file exchange and subsequently subdivide it through Loop's subdivision algorithm by using Paraview [53]. The phase field is represented as a colormap on the reference configuration, see Figs. 10A,C. Figures 10B,D shows the physical deformation obtained, which has been amplified by a factor of 20 to give a better idea of the resulting displacements. Due to the nonlinearity of the model, we observe a symmetry-breaking solution.

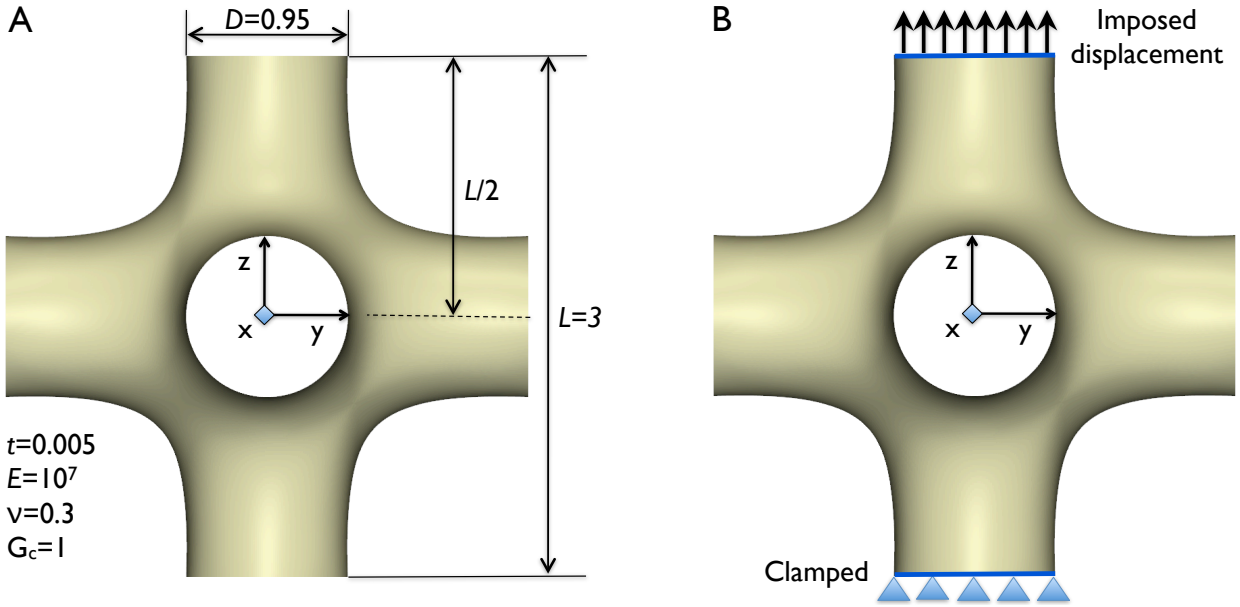


Figure 9: Sketch for the brittle thin shell problem. (A) Material and geometrical parameters describing a set of six connected open pipes. (B) The prescribed boundary conditions and the applied incremental displacement.

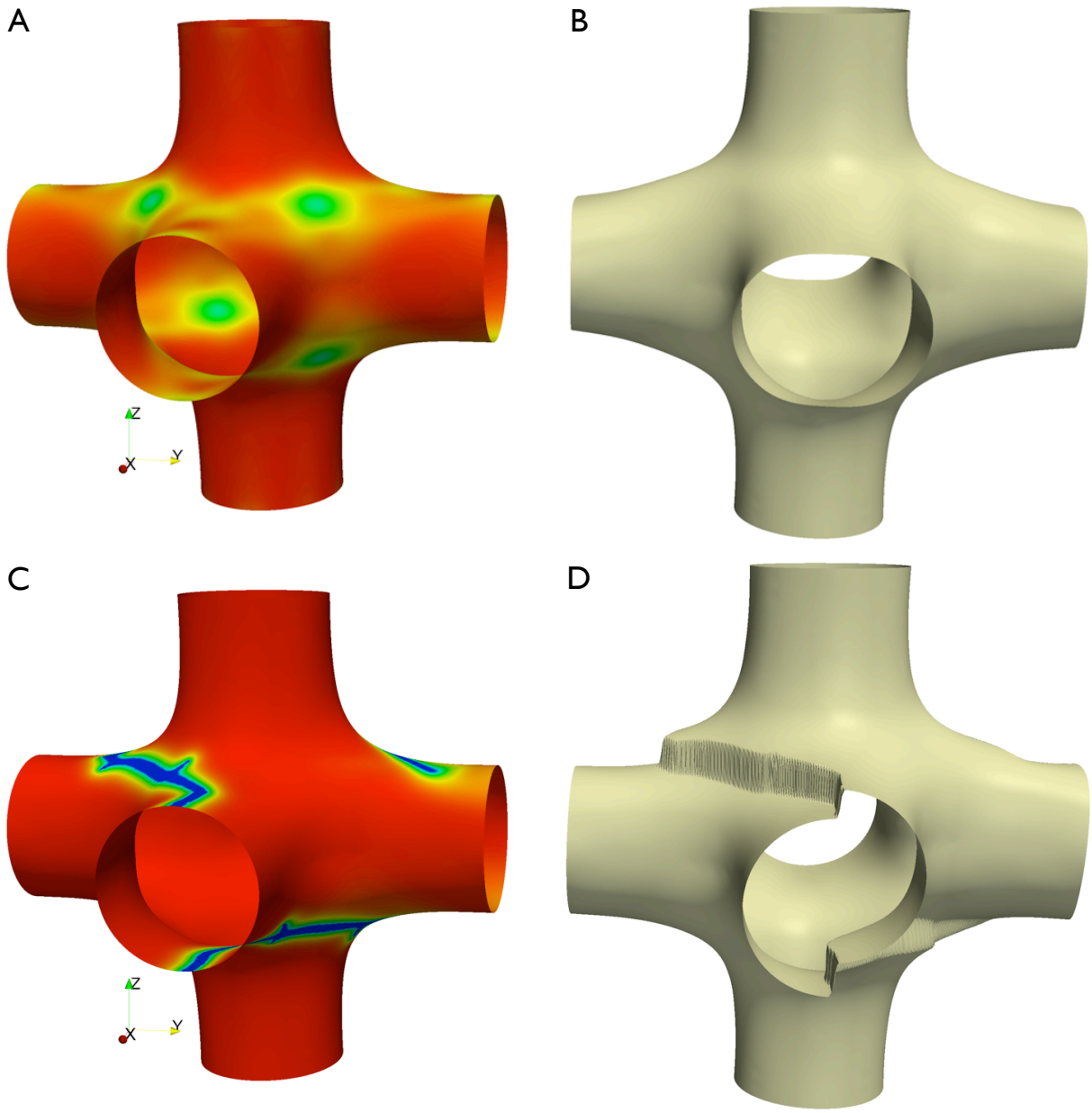


Figure 10: Selected snapshots of the deformation process of a brittle thin shell with complex topology. The boundary curve of the bottom pipe is clamped and the top boundary curve is incrementally displaced in the upward $(0, 0, 1)$ direction. The process has been performed without an initial crack. (A,C) Phase field as colormap in the reference configuration for two selected imposed displacements of the top boundary curve, just before the fracture ($d = 0.0055$) and for the final imposed displacement, $d = 0.01$. (B,D) Deformed configurations for two selected instants, the deformation field has been magnified by 20.

# 6 Conclusions

We have extended the methodology proposed in [21] to model fracture in Kirchhoff- Love thin shell bodies described by surface of complex geometry and topology. We developed this method for brittle material and analyzed this model for a structure with complex geometry and topology. Simulations have shown that the onset of crack propagation in the phase-field model can be linked to the energy release rate reaching the critical value $G_c$.

It is noteworthy in this work that we have used different values of the LME aspect parameter $\gamma$, for both phase-field and thin shell model. We observe that by using similar LME approximants (equal $\gamma$) leads to less accurate results for phase-field. Additionally, different parameters $\gamma$ make impossible to obtain rights results for mode II, due to connection between shape functions on both sides of crack. The future work is to use equals values of the smoothness LME parameter $\gamma$ for both problems by introducing a higher order phase-field model. Our current research includes developing a fourth order phase-field model to use in conjunction with smooth approximants as LME or Isogeometric, the aim is to increase the order of convergence, and improve the accuracy and efficiency.

# Acknowledgements

DM and MA acknowledge the support of the European Research Council under the European Community's 7th Framework Programme (FP7/2007-2013)/ERC grant agreement nr 240487. MA acknowledges the support received through the prize "ICREA Academia" for excellence in research, funded by the Generalitat de Catalunya. FA and TR would like to thank the DAAD Programme des Projektbezogenen Personenaustauschs, for financial support to trip to Spain, and the Free State of Thuringia and Bauhaus Research School for financial support during the duration of this project . YS would like to acknowledge the support of the grant from Subprograma *Acciones Integradas España-Alemania* (Spanish Ministry of Science and Innovation) with reference number PRI-AIBDE-2011-0883.

# References

[1] T. Rabczuk and T. Belytschko, "Cracking particles: a simplified meshfree method for arbitrary evolving cracks," *International Journal for Numerical Methods in Engineering*, vol. 61, no. 13, pp. 2316–2343, 2004.

[2] T. Rabczuk and G. Zi, "A meshfree method based on the local partition of unity for cohesive cracks," *Computational Mechanics*, vol. 39, no. 6, pp. 743–760, 2007.

[3] L. Chen, T. Rabczuk, S. Bordas, G. Liu, K. Zeng, and P. Kerfriden, "Extended finite element method with edge-based strain smoothing (esm-xfem) for linear elastic crack growth," *Computer Methods in Applied Mechanics and Engineering*, vol. 209 - 212, no. 0, pp. 250 – 265, 2012.

[4] T. Rabczuk, "Computational methods for fracture in brittle and quasi-brittle solids: State-of-the-art review and future perspectives," *ISRN Applied Mathematics*, vol. 2013, p. 38, 2013.

[5] F. Amiri, C. Anitescu, M. Arroyo, S. Bordas, and T. Rabczuk, "Xlme interpolants, a seamless bridge between xfem and enriched meshless methods," *Computational Mechanics*, pp. 1–13, 2013.

[6] J. Dolbow, N. Moës, and T. Belytschko, "Modeling fracture in mindlin-reissner plates with the extended finite element method," *International Journal of Solids and Structures*, vol. 37, pp. 7161–7183, 1999.

[7] P. Baiz, S. Natarajan, S. Bordas, P. Kerfriden, and T. Rabczuk, "Linear buckling analysis of cracked plates by sfem and xfem (smxfem)," *Journal of Mechanics of Materials and Structures*, vol. 9, pp. 1213–1238, 2011.

[8] S. Natarajan, P. Baiz, S. Bordas, T. Rabczuk, and P. Kerfriden, "Natural frequencies of cracked functionally graded material plates by the extended finite element method," *Composite Structures*, vol. 93, no. 11, pp. 3082 – 3092, 2011.

[9] X. Zhuang, R. Huang, H. Zhu, H. Askes, and K. Mathisen, "A new and simple locking-free triangular thick plate element using independent shear degrees of freedom," *Finite Elements in Analysis and Design*, vol. 75, no. 0, pp. 1 – 7, 2013.

[10] P. M. A. Areias and T. Belytschko, "Non-linear analysis of shells with arbitrary evolving cracks using xfem," *International Journal for Numerical Methods in Engineering*, vol. 62, no. 3, pp. 384–415, 2005.

[11] P. Areias, J. Song, and T. Belytschko, "Analysis of fracture in thin shells by overlapping paired elements," *Computer Methods in Applied Mechanics and Engineering*, vol. 195, no. 41–43, pp. 5343 – 5360, 2006.

[12] T. Chau-Dinh, G. Zi, P.-S. Lee, T. Rabczuk, and J.-H. Song, "Phantom-node method for shell models with arbitrary cracks," *Computers and Structures*, vol. 92–93, no. 0, pp. 242 – 256, 2012.

[13] F. Cirak, M. Ortiz, and A. Pandolfi, "A cohesive approach to thin-shell fracture and fragmentation," *Computer Methods in Applied Mechanics and Engineering*, vol. 194, no. 21–24, pp. 2604 – 2618, 2005.

[14] T. Rabczuk and P. Areias, "A meshfree thin shell for arbitrary evolving cracks based on an extrinsic basis," *Computer Modeling in Engineering and Sciences*, vol. 16, no. 2, pp. 115–130, 2006.

[15] T. Rabczuk, P. Areias, and T. Belytschko, "A meshfree thin shell method for non-linear dynamic fracture," *International Journal for Numerical Methods in Engineering*, vol. 72, no. 5, pp. 524–548, 2007.

[16] T. Rabczuk, R. Gracie, J.-H. Song, and T. Belytschko, "Immersed particle method for fluidstructure interaction," *International Journal for Numerical Methods in Engineering*, vol. 81, no. 1, pp. 48–71, 2010.

[17] X. Zhuang, C. Augarde, and K. Mathisen, "Fracture modeling using meshless methods and level sets in 3d: Framework and modeling," *International Journal for Numerical Methods in Engineering*, vol. 92, no. 11, pp. 969–998, 2012.

[18] S. Wu, G. Li, and T. Belytschko, "A dkt shell element for dynamic large deformation analysis," *Communications in Numerical Methods in Engineering*, vol. 21, no. 11, pp. 651–674, 2005.

[19] P. Areias and T. Belytschko, "Analysis of finite strain anisotropic elastoplastic fracture in thin plates and shells," *Journal of Aerospace Engineering*, vol. 19, no. 4, pp. 259–270, 2006.

[20] G. Becker and L. Noels, "A full-discontinuous galerkin formulation of nonlinear kirchhoff–love shells: elasto-plastic finite deformations, parallel computation, and fracture applications," *International Journal for Numerical Methods in Engineering*, vol. 93, no. 1, pp. 80–117, 2013.

[21] D. Millán, A. Rosolen, and M. Arroyo, "Nonlinear manifold learning for meshfree finite deformations thin shell analysis," *International Journal for Numerical Methods in Engineering*, vol. 93, no. 7, pp. 685–713, 2013.

[22] Y. CAI, X. ZHUANG, and H. ZHU, "A generalized and efficient method for finite cover generation in the numerical manifold method," *International Journal of Computational Methods*, vol. 10, no. 05, p. 1350028, 2013.

[23] H. Gomez, V. Calo, Y. Bazilevs, and T. Hughes, "Isogeometric analysis of the Cahn-Hilliard phase-field model," *Computer Methods in Applied Mechanics and Engineering*, vol. 197, pp. 4333–4352, 2008.

[24] H. Gomez, T. Hughes, X. Nogueira, and V. Calo, "Isogeometric analysis of the isothermal Navier-Stokes-Korteweg equations," *Computer Methods in Applied Mechanics and Engineering*, vol. 199, pp. 1828–1840, 2010.

[25] A. Abdollahi and I. Arias, "Phase-field modeling of the coupled microstructure and fracture evolution in ferroelectric single crystals," *Acta Materialia*, vol. 59, no. 12, pp. 4733 – 4746, 2011.

[26] A. Rosolen, C. Peco, and M. Arroyo, "An adaptive meshfree method for phase-field models of biomembranes. part i: Approximation with maximum-entropy basis functions," *Journal of Computational Physics*, vol. 249, no. 0, pp. 303 – 319, 2013.

[27] G. Francfort and J.-J. Marigo, "Revisiting brittle fracture as an energy minimization problem," *Journal of the Mechanics and Physics of Solids*, vol. 46, pp. 1319–1342, 1998.

[28] B. Bourdin, G. Francfort, and J.-J. Marigo, "The Variational Approach to Fracture," *Journal of Elasticity*, vol. 91, no. 1-3, pp. 5–148, 2008.

[29] M. L. Bucalem and K.-J. Bathe, "Higher-order mitc general shell elements," *International Journal for Numerical Methods in Engineering*, vol. 36, no. 21, pp. 3729–3754, 1993.

[30] J. Simo and D. Fox, "On a stress resultant geometrically exact shell model. Part I: Formulation and optimal parametrization," *Computer Methods in Applied Mechanics and Engineering*, vol. 72, pp. 267–304, 1989.

[31] P. Krysl and T. Belytschko, "Analysis of thin shells by the element-free galerkin method," *International Journal of Solids and Structures*, vol. 33, no. 2022, pp. 3057 – 3080, 1996.

[32] L. Noels and R. Radovitzky, "A new discontinuous galerkin method for kirchhofflove shells," *Computer Methods in Applied Mechanics and Engineering*, vol. 197, no. 3340, pp. 2901 – 2929, 2008.

[33] G. Becker, C. Geuzaine, and L. Noels, "A one field full discontinuous galerkin method for kirchhofflove shells applied to fracture mechanics," *Computer Methods in Applied Mechanics and Engineering*, vol. 200, no. 4546, pp. 3223 – 3241, 2011.

[34] F. Cirak and Q. Long, "Subdivision shells with exact boundary control and non-manifold geometry," *International Journal for Numerical Methods in Engineering*, vol. 88, no. 9, pp. 897–923, 2011.

[35] J. Kiendl, K.-U. Bletzinger, J. Linhard, and R. Wüchner, "Isogeometric shell analysis with kirchhoff–love elements," *Computer Methods in Applied Mechanics and Engineering*, vol. 198, no. 49–52, pp. 3902 – 3914, 2009.

[36] D. Benson, Y. Bazilevs, M. Hsu, and T. Hughes, "Isogeometric shell analysis: The reissner–mindlin shell," *Computer Methods in Applied Mechanics and Engineering*, vol. 199, no. 5–8, pp. 276 – 289, 2010.

[37] N. Nguyen-Thanh, J. Kiendl, H. Nguyen-Xuan, R. Wüchner, K. Bletzinger, Y. Bazilevs, and T. Rabczuk, "Rotation free isogeometric thin shell analysis using pht-splines," *Computer Methods in Applied Mechanics and Engineering*, vol. 200, no. 47–48, pp. 3410 – 3424, 2011.

[38] D. Millán, A. Rosolen, and M. Arroyo, "Thin shell analysis from scattered points with maximum-entropy approximants," *International Journal for Numerical Methods in Engineering*, vol. 85, no. 6, pp. 723–751, 2011.

[39] M. Arroyo and M. Ortiz, "Local maximum-entropy approximation schemes: a seamless bridge between finite elements and meshfree methods," *International Journal for Numerical Methods in Engineering*, vol. 65, no. 13, pp. 2167–2202, 2006.

[40] A. Rosolen, D. Millán, and M. Arroyo, "On the optimum support size in meshfree methods: a variational adaptivity approach with maximum entropy approximants," *International Journal for Numerical Methods in Engineering*, vol. 82, no. 7, pp. 868–895, 2010.

[41] D. Levin, "Mesh-independent surface interpolation," in *Geometric Modeling for Scientific Visualization* (H. Brunnett and Mueller, eds.), pp. 37–49, Springer-Verlag, 2003.

[42] F. Cirak, M. Ortiz, and P. Schröder, "Subdivision surfaces: a new paradigm for thin-shell finite-element analysis," *International Journal for Numerical Methods in Engineering*, vol. 47, no. 12, pp. 2039–2072, 2000.

[43] F. Cirak and M. Ortiz, "Fully $C^1$-conforming subdivision elements for finite deformation thin-shell analysis," *International Journal for Numerical Methods in Engineering*, vol. 51, no. 7, pp. 813–833, 2001.

[44] J. Simo, D. Fox, and M. Rifai, "On a stress resultant geometrically exact shell model. Part II: the linear theory; computational aspects," *Computer Methods in Applied Mechanics and Engineering*, vol. 73, pp. 53–92, 1989.

[45] H. Amor, J.-J. Marigo, and C. Maurini, "Regularized formulation of the variational brittle fracture with unilateral contact: Numerical experiments," *Journal of the Mechanics and Physics of Solids*, vol. 57, no. 8, pp. 1209–1229, 2009.

[46] C. Miehe, F. Welschinger, and M. Hofacker, "Thermodynamically consistent phase-field models of fracture: Variational principles and multi-field fe implementations," *International Journal for Numerical Methods in Engineering*, vol. 83, pp. 1273–1311, 2010.

[47] B. Bourdin, "Numerical implementation of the variational formulation for quasi-static brittle fracture," *Interfaces and Free Boundaries*, vol. 9, no. 3, pp. 411–430, 2007.

[48] T. Rabczuk, S. P. Xiao, and M. Sauer, "Coupling of mesh-free methods with finite elements: basic concepts and test results," *Communications in Numerical Methods in Engineering*, vol. 22, no. 10, pp. 1031–1065, 2006.

[49] V. P. Nguyen, T. Rabczuk, S. Bordas, and M. Duflot, "Meshless methods: A review and computer implementation aspects," *Mathematics and Computers in Simulation*, vol. 79, no. 3, pp. 763 – 813, 2008.

[50] Y. Cai, X. Zhuang, and C. Augarde, "A new partition of unity finite element free from the linear dependence problem and possessing the delta property.," *Computer methods in applied mechanics and engineering.*, vol. 199, pp. 1036–1043, January 2010.

[51] N. Vu-Bac, H. Nguyen-Xuan, L. Chen, C. K. Lee, G. Zi, X. Zhuang, G. R. Liu, and T. Rabczuk, "A phantom-node method with edge-based strain smoothing for linear elastic fracture mechanics," *Journal of Applied Mathematics*, p. 12, 2013.

[52] X. Zhuang, H. Zhu, and C. Augarde, "An improved meshless shepard and least squares method possessing the delta property and requiring no singular weight function," *Computational Mechanics*, pp. 1–15, 2013.

[53] A. Henderson, *The ParaView Guide: A Parallel Visualization Application*. Kitware Inc., 2007.